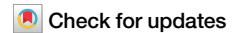


<https://doi.org/10.1038/s42003-025-08371-7>

Site- and cell-type-specific miRNA and mRNA genes and networks across the cortex, striatum, and hypothalamus



Amanda M. Zacharias¹, Ciara D. O'Connor¹, Danai G. Topouza¹, Zhi Yi Fang¹,
Helia Ghazinejad^{1,2}, Hanlin Chen^{1,2}, Qingling Duan^{1,2,5} ✉ & Nader Ghasemlou^{1,3,4,5} ✉

Biological rhythms control gene expression, but effects on central nervous system (CNS) cells and structures remain poorly defined. While circadian (24-hour) rhythms are most studied, many genes have periods of greater and less than 24-hours; these fluctuations can be both site- and cell-specific. Identifying patterns of gene rhythmicity across the CNS is necessary for both the study of chronobiology and to make sense of data obtained in the laboratory. We now identify cycling mRNAs, miRNAs, gene networks and mRNA-miRNA co-expression pairs in the cortex, hypothalamus, and corpus striatum of male C57BL/6J mice using high-dimensional datasets. A searchable catalogue (<https://www.ghasemloulab.ca/chronoCNS>) helps refine the analysis of cellular and molecular rhythmicity across the CNS (using the liver as a control). Immunofluorescence confirms the rhythmicity of key targets across cells in these structures, with strong cycling signatures in resting oligodendrocytes. Our study sheds light on the contribution of diurnal, ultradian, and infradian rhythms and mRNA-miRNA interactions to CNS function.

Circadian rhythms are 24-h endogenous processes that help organisms adapt to the transition between day and night. Transcription-translation loops govern these processes through clock genes, which regulate the expression of genes in a tissue- and cell-specific manner to drive various outcomes¹. Emerging evidence from naïve and disease states suggests that rhythms are integral to CNS function and activity. For example, the hypothalamus controls circadian activity via hormone secretion²; this rhythmicity affects outcomes including cognition and memory (e.g., in the cerebral cortex)³, and goal-directed behavior (e.g., in the striatum)⁴. These sites not only have distinct functions, but also highly specific gene expression that represent over 5000 cell clusters⁵. Gaining an understanding of when and where gene expression changes across the naïve CNS is fundamental to our understanding of neurobiological outcomes; therefore, there is a need for more detailed profiling of gene rhythmicity and gene-gene interactions across CNS sites.

Circadian (24-h) rhythms govern most cycling genes, though ultradian (<24-h) and infradian (>24-h) periods are also possible⁶. The suprachiasmatic nucleus of the hypothalamus synchronizes these rhythms. A foundational study estimated that ~40% of the mouse protein-coding genome has a circadian rhythm in at least one of 12 organs—including the

brainstem, cerebellum, and hypothalamus—though only 10 genes were found to be cycling across all organs, of which seven were core clock components⁷. Interestingly, it was found that 16% of genes in the liver (considered to be among the most rhythmic organs) were under circadian control, while the CNS sites studied had less than 4% rhythmic genes⁷. Similar low levels of cycling gene expression have been found in the striatum (5%)⁸ and forebrain cortex (6%)⁹. Ultradian gene expression was first comprehensively described in the mouse liver, revealing a small subset of genes with periods of either 8- or 12-h¹⁰. More recent analysis found that 6% of transcripts in the human prefrontal cortex have a 12-h period, which can be altered in neurological disease¹¹. Previous work has observed infradian rhythms among genes, often exemplified by variations in menstrual and seasonal cycles⁶. However, there are few studies of gene rhythms for periods between 24- and 48-h in the CNS or other organs/tissues. Beyond needing to elucidate the dynamics of cycling gene tissue specificity and variable cycling periods in the naïve CNS, post-transcriptional regulation of these genes adds yet another complex variable to consider in CNS gene expression.

There is a discrepancy between rhythmic transcripts and proteins in the brain and liver^{9,12}, suggesting that post-transcriptional/translational regulators generate rhythmicity; miRNAs are key post-transcriptional

¹Department of Biomedical and Molecular Sciences, Queen's University, Kingston, ON, Canada. ²School of Computing, Queen's University, Kingston, ON, Canada. ³Department of Anesthesiology and Perioperative Medicine, Queen's University, Kingston, ON, Canada. ⁴Centre of Neuroscience Studies, Queen's University, Kingston, ON, Canada. ⁵These authors contributed equally: Qingling Duan, Nader Ghasemlou. ✉ e-mail: qingling.duan@queensu.ca; nader.ghasemlou@queensu.ca

regulators that may contribute to this phenomenon. These short RNAs typically bind to the 3' untranslated region of mRNAs, leading to decreased mRNA stability and protein production. Through this function, miRNAs play important roles in neuroplasticity and neurodegenerative diseases¹³. Moreover, miRNAs have cycling rhythms of expression across the mouse transcriptome^{14,15}, and are thought to modify the rhythmic characteristics of mRNAs^{14,16}. Furthermore, miRNAs act in a highly tissue-specific manner, which may explain the tissue-specificity of circadian gene expression¹⁷.

We therefore hypothesized that CNS rhythmicity would occur differentially across CNS regions and cell types, and that cycling genes would be co-expressed. Taking advantage of a transcriptomic dataset of 6-month-old male C57BL/6J mouse cortex, hypothalamus, striatum, and liver collected every 3-h over 36-h in a 12:12 light-dark environment, our work identifies site-specific cycling genes in the CNS and works towards uncovering their impact in the naïve state. Potential interactions between cycling mRNAs and miRNAs, whose post-transcriptional regulation of rhythmic genes may be tissue-specific, are also revealed. Finally, we describe clusters of cycling genes and their approximate cellular composition. We validate our findings using cell-specific protein expression. Our results build a foundation upon which potential molecular/cellular circadian gene networks and interactions can be identified across the CNS, which we now provide as a searchable database.

Results

Distinct biological rhythms of mRNAs and miRNAs across CNS sites

We began by identifying cyclic mRNAs and miRNAs in tissues collected from the naïve cerebral cortex, hypothalamus, and striatum, with the liver used as a positive control (Supplementary Fig. 1; “Methods”). Bioinformatic guidelines¹⁸ to detect rhythmic gene expression were employed for this analysis using the R packages *MetaCycle*¹⁹, to detect genes with a 24-h period and both *RAIN*²⁰ and *ARSER*²¹, to detect non-24-h rhythms. The cortex had the highest number of cycling mRNAs among CNS tissues (Fig. 1a; Supplementary Data 1). As expected⁷, the liver had the most 24-h cycling mRNAs overall. However, the cortex had the most rhythmic genes when considering non-24-h period mRNAs. To confirm our results, we compared cycling genes detected by *MetaCycle* and *RAIN*; all genes identified using *MetaCycle* were also identified using *RAIN* for analysis (Fig. 1b). Moreover, the periods for these overlapping mRNAs were largely estimated to be 24 ± 3 -h by *RAIN*, showing concordance between the algorithms (Fig. 1c). There was up to a >5-fold increase in the number of cycling mRNAs identified among CNS sites (with only a ~20% change in the liver) when using *RAIN*, suggesting an increased presence of non-24-h rhythmic genes in the CNS.

While most cycling genes appear diurnal, ultradian and infradian periods were also present in the CNS. As shown by others^{10,19}, we found the period of liver mRNAs clustered around 12-, 24-, and >24-h (Fig. 1d; Supplementary Fig. 2-4). While these patterns also appear (though to a lesser extent) in the CNS, most genes exhibited a 24 ± 3 -h period (Fig. 1d). As estimated by *MetaCycle*, mRNA phases across the CNS (but not the liver) appeared to exhibit a bimodal distribution, with high numbers of cycling genes at ~ZT 6–12 and 18–24; this distribution was not observed in the CNS or liver in phase estimates by *RAIN* (Fig. 1e). Relative amplitudes had a wide range across tissues, with the liver having the greatest range, whereas the CNS was more restricted (Fig. 1f). We focused on the key clock genes (Supplementary Fig. 5) and confirmed that their expression followed a 24-h period. Among core clock genes, the transcription factor *Bhlhe41* was rhythmic across CNS sites but not in the liver; *Adrb1* was only cycling in the cortex; *Timeless* and *Ruvbl2*, a newly-discovered core circadian clock gene²², were only rhythmic in the liver.

Using *MetaCycle*, only eight cycling miRNAs were identified in at least one site (miR-5099, miR-124a-2, miR-342, miR-150, miR-29b-1, miR16-1, miR-6539, and miR-223), consistent with previous studies showing few

cycling miRNAs (Fig. 1g)^{7,14,23,24}. As with our mRNA analysis, more cycling miRNAs were identified using *RAIN* than *MetaCycle* (Fig. 1h). We also saw concordance between *MetaCycle* and *RAIN* (Fig. 1i). Most miRNAs exhibited a 24 ± 3 -h period (Fig. 1j), and miRNA phases did not exhibit a consistent pattern across tissues (Fig. 1k). Relative amplitudes of miRNAs ranged from 0.1 to 0.5 (Fig. 1l). The proportions of genes changing across CNS sites align with previous studies^{7-9,19,25}, though results obtained using *ARSER* found an unexpectedly high proportion of genes to be cycling (Supplementary Fig. 6). Thus, our use of a broader range of cycling periods, improved data resolution, and tissue collected from mice entrained to a 12:12 light-dark cycle during sample analysis identified, to the best of our knowledge, new genes that are cycling in the CNS.

Specificity of cycling genes in three CNS structures

We next assessed the site-specificity of detected cycling genes by focusing on the results obtained using *RAIN*, given that 24-h and non-24-h rhythms are captured; *MetaCycle* results are presented in Supplementary Fig. 7. Relatively few genes were cycling in all four tissues (Fig. 2a; mRNA = 1332; miRNA = 1, miR-5099), with the liver containing the most unique cycling genes and the striatum the fewest. In addition to the 1332 mRNAs cycling across all tissues, 781 mRNAs were cycling across all CNS sites, again with only miR-5099 showing rhythmicity among miRNAs. Many of these genes exhibited different cycling parameters depending on the site assessed (Supplementary Data 2). We identified 7391 mRNAs with period differences ranging between 3- and 21-h across sites (Fig. 2b); phase differences between any two CNS sites for 7235 mRNAs, of which 3955 had an absolute difference ≥ 6 -h and 1131 were in antiphase (12 ± 3 -h; Fig. 2c). Finally, 495 shared CNS genes were identified with relative amplitudes up to 0.71 (Fig. 2d).

It has been suggested that differential expression and/or rhythmicity of regulatory factors (e.g., transcription factors or miRNAs) across sites could account for site- or tissue-dependent cycling parameters^{7,26}. In support of this mechanism, pathway analysis of mRNAs with both large period (≥ 9 -h) and phase (12 ± 3 -h) differences between tissues identified the binding motif for transcription factor gene *E2f3* as being significantly enriched (Supplementary Fig. 8). This gene was cycling only in the cortex and hypothalamus, and had varying phases and periods between these sites. *E2f3* had a phase of 3 in the cortex but 15 in the hypothalamus, and a period of 12-h and 21-h, respectively, in these sites (Fig. 3). Further, previous work has shown that deletion of *CRY2* upregulates the expression of genes targeted by factors in the E2F family²⁷.

Cycling genes are linked to human chronotype genetics

Given that cycling mRNAs identified by *MetaCycle* are estimated to have a 24-h period and thus may be under circadian control, we assessed their overlap with 366 genes previously linked to human chronotype²⁸. Of these, cycling genes were overlapping in the cortex ($n = 107$, $P_{BH} = 1$), hypothalamus ($n = 39$, $P_{BH} = 1$), striatum ($n = 10$, $P_{BH} = 1$), and liver ($n = 128$, $P_{BH} = 1$). Only *Rbm6*, *Fbxl4*, *Rfx4*, *Ahsa2*, and *Hexim1* were shared across all CNS sites (Supplementary Data 3). Transcription corepressor binding and circadian rhythm/entrainment were key pathways identified among chronotype genes, though no pathways were shared across all CNS sites (Supplementary Fig. 9; Supplementary Data 4). These genes may be critical to chronotype, which varies across mouse strains²⁹⁻³¹.

Shared and unique pathways across the CNS and period categories

Analysis of cycling mRNAs from *RAIN* found protein folding, cell migration, and RNA modification as shared pathways in the CNS and liver (Fig. 4a; Supplementary Data 5); those unique to the CNS included axonogenesis, learning or memory, mRNA stabilization, and macrophage differentiation (Fig. 4b-d; Supplementary Data 6), while ribosomal and metabolic pathways were unique to the liver (Fig. 4e; Supplementary Data 7). We identified pathways uniquely enriched across period categories.

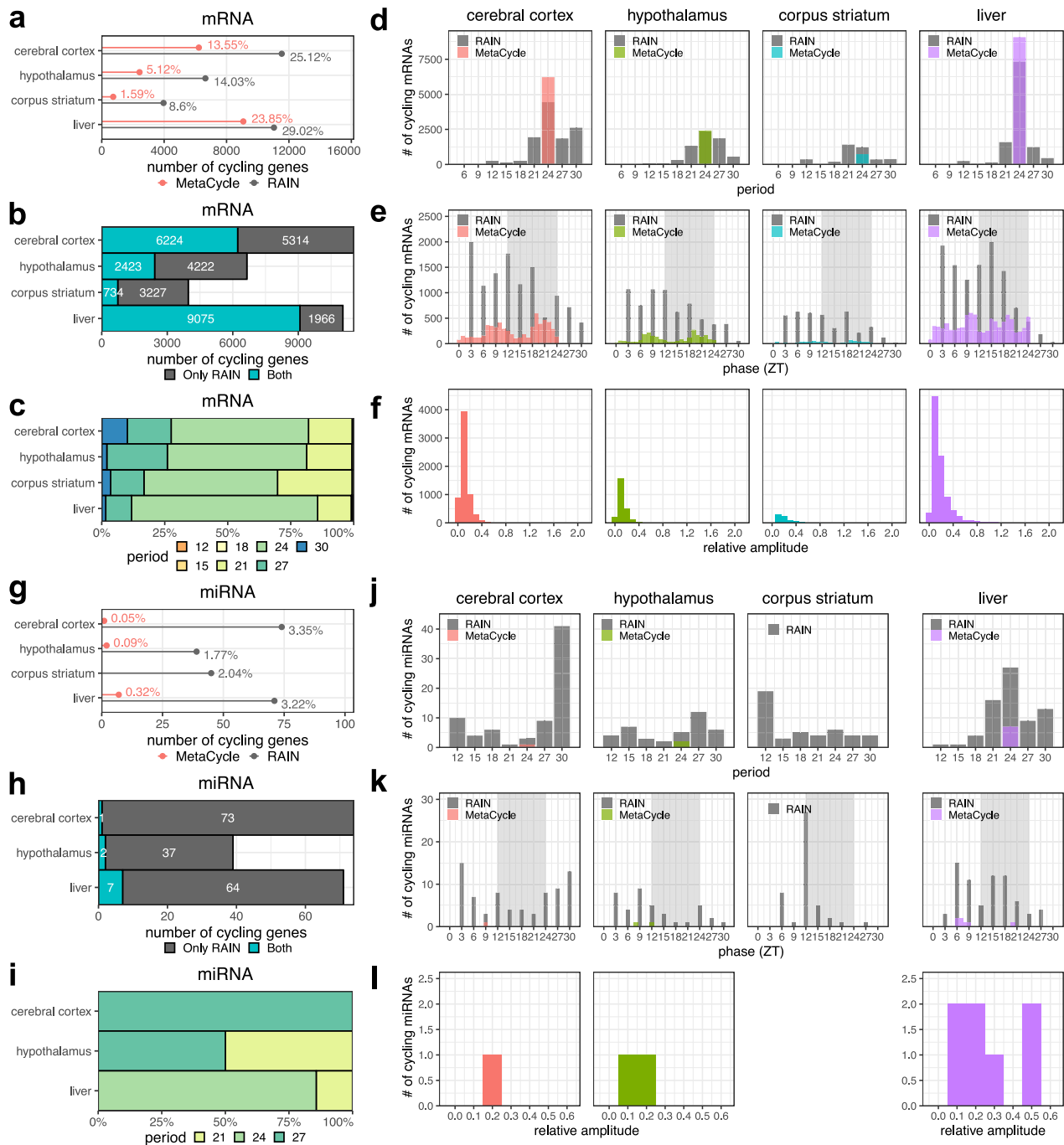


Fig. 1 | Variability in the number, period, phase, and relative amplitude of cycling mRNAs and miRNAs across CNS tissues. a–f mRNAs, **g–l** miRNAs. **a, g** The number (x -axis; $P_{BH} < 0.05$) and percentage (listed in plots) of cycling genes in each CNS tissue, with results using both *MetaCycle* (red) and *RAIN* (grey). **b, h** Overlap of the numbers of genes detected by only *RAIN* (grey) or both *MetaCycle* and *RAIN* (turquoise). **c, i** The distribution of period lengths (hours) predicted by *RAIN*

amongst cycling genes also detected by *MetaCycle*. Cycling parameters estimated in the cerebral cortex (red), hypothalamus (green), corpus striatum (turquoise), and liver (purple) using *MetaCycle* and *RAIN* (grey). **d, j** Distribution of period lengths between 6 and 30-h. **e, k** Distribution of phases between Zeitgeber Time 0 and 30, with entrained darkness highlighted with a grey background. **f, l** The distribution of relative amplitudes from 0.015 to 2.03.

Pathways involving autophagy, protein folding, and cellular stress were unique to the mRNAs with a 24 ± 3 -h period and appeared in both the CNS and liver (Fig. 5a–d; Supplementary Data 8). Pathways identified in the cerebral cortex and corpus striatum with periods of 12 ± 3 -h include extracellular matrix binding and Hippo signaling (Fig. 5e, f), while liver mRNAs with 12 ± 3 -h periods were enriched in the endoplasmic reticulum and Golgi processes (Fig. 5g), aligning with existing literature^{10,32}. CNS-specific pathways with 28–30-h periods included pre- and post-synaptic membrane and retinoic acid-inducible gene 1 (RIG-1) binding pathways

(Fig. 5h–j), while 28–30-h period liver mRNAs were enriched in pathways related to innate immunity (Fig. 5k).

miRNAs with a 24 ± 3 -h period were enriched for pathways involved in retinal cell development, response to inhibitory leukemia factor, sensory perception of mechanical stimulus, and sensory perception of sound (Fig. 6a–c), while 12 ± 3 -h period miRNAs were involved in synaptic signaling and cellular response to alcohol (Fig. 6d–f). Synaptic potentiation/plasticity, response to forskolin, and energy homeostasis were key pathways for the 28–30-h period miRNAs (Fig. 6g–i).

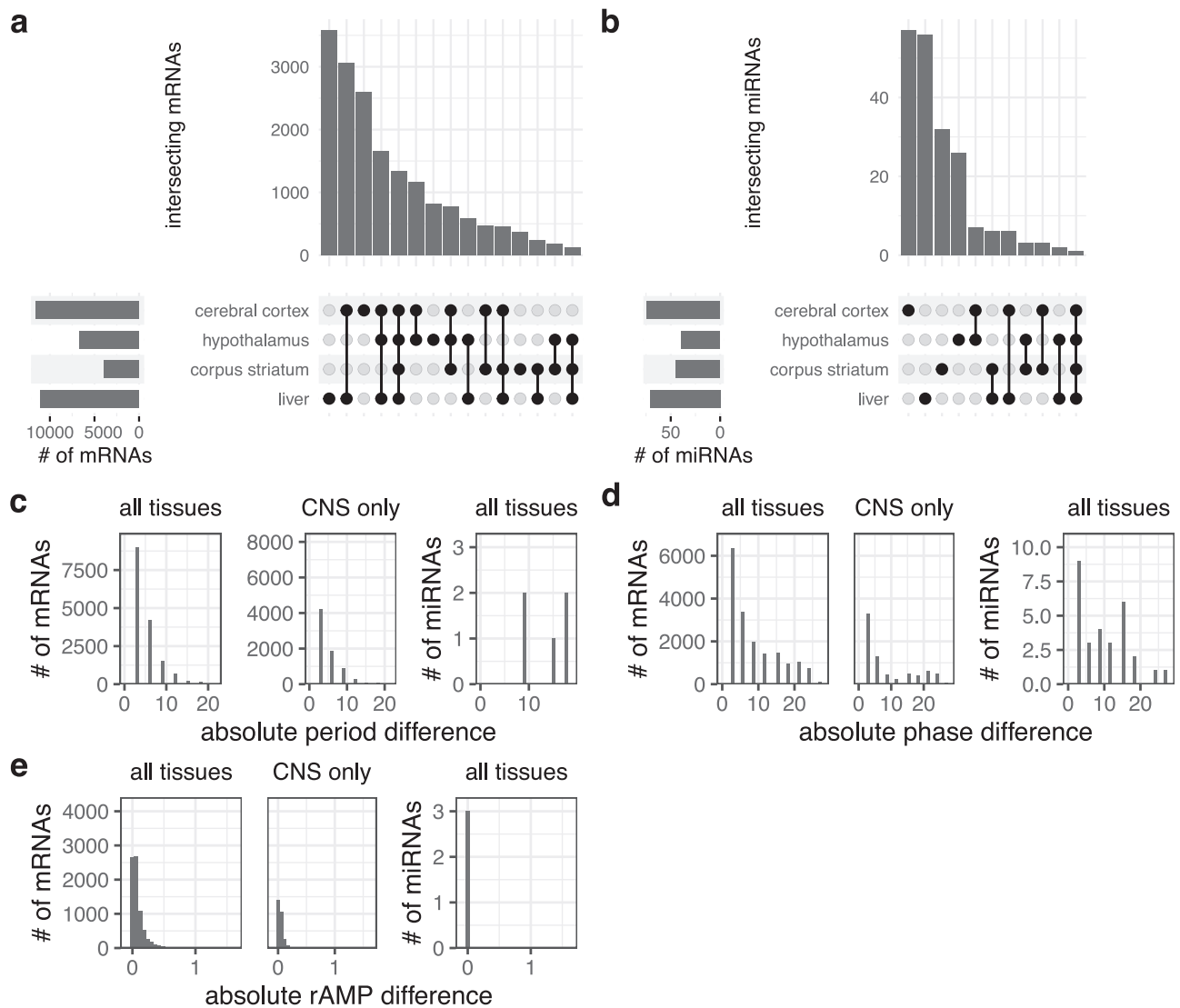


Fig. 2 | Comparison of cycling genes across tissues. a Intersections of cycling mRNAs from RAIN across cycles. **b** Intersections of cycling miRNAs from RAIN across cycles. Distributions of cycling parameter differences between tissues. **c, d** Period and phase estimated by RAIN. **e** Relative amplitude estimated by MetaCycle.

Identification of mRNA–miRNA pairs and pathways across the CNS

We next tested for associations between 24-h cycling mRNA–miRNA pairs in the CNS. This yielded 5618 pairs in the cortex and 2533 in the hypothalamus ($P_{BH} < 0.05$). The striatum could not be included in the analysis, given the lack of 24-h cycling miRNAs. The liver, with its many cycling genes, contained 42,659 mRNA–miRNA pairs ($P_{BH} < 0.05$). Putative direct control of mRNA expression by miRNAs was identified, using a negative correlation and delay ≤ 0 , in ~50% of pairs in the CNS and ~25% in the liver (Supplementary Data 9), suggesting that miRNAs may play a more important role in CNS rhythmicity than they would in the liver. Of the direct interaction pairs, only a small subset has been previously predicted or experimentally validated (Fig. 7; Supplementary Data 10, 11), highlighting the need for further study of miRNA regulation of diurnal gene expression. Previously predicted but unvalidated direct mRNA–miRNA cycling pairs may present new targets for assessing post-transcriptional regulation of CNS rhythmicity.

Since genes work in concert to influence complex biological functions, we used network analysis to identify co-expression modules of mRNAs and miRNAs separately (Supplementary Fig. 10, 11; “Methods”). Cycling mRNAs were enriched in 12 of 26 modules in the cortex, 7 of 15 in the hypothalamus, 9 of 13 in the striatum, and 7 of 20 in the liver (Figs. 8a, b; 12);

the majority of hub genes in these modules were rhythmic. Cycling miRNAs identified using RAIN were found in all modules except the striatal green module, while those identified using MetaCycle were found in 1 of 4 modules in the cortex, 2 of 3 in the hypothalamus, and 3 of 3 in the liver (Fig. 8c, d). Visualizing the composition of cycling genes and their period categories within modules showed that most modules contain genes with a period of 24 ± 3 -h (Supplementary Figs. 12, 13). However, there were some exceptions: for example, the cortical *yellow4* module has few non-cycling mRNAs, of which most have a period of 27-h or greater. Finally, analysis of cycling module eigengenes showed that 33 of 126 mRNA–miRNA module pairs were associated ($P_{BH} < 0.05$; Supplementary Fig. 14). Altogether, our study identifies modules of coordinated rhythmic gene expression in the CNS.

Cycling genes contribute to neuroimmune interactions in the healthy state

The CNS is a complex organ that includes neuronal, glial, and supporting cells. Thus, we examined the cellular composition of cycling mRNA modules that are typically thought to represent distinct cell types, although recent evidence shows heterogeneous modules in the striatum²⁵. CNS cell marker genes were enriched in 8 cycling modules in the cortex, 1 in the hypothalamus, and 3 in the striatum; as expected, none were enriched in the liver

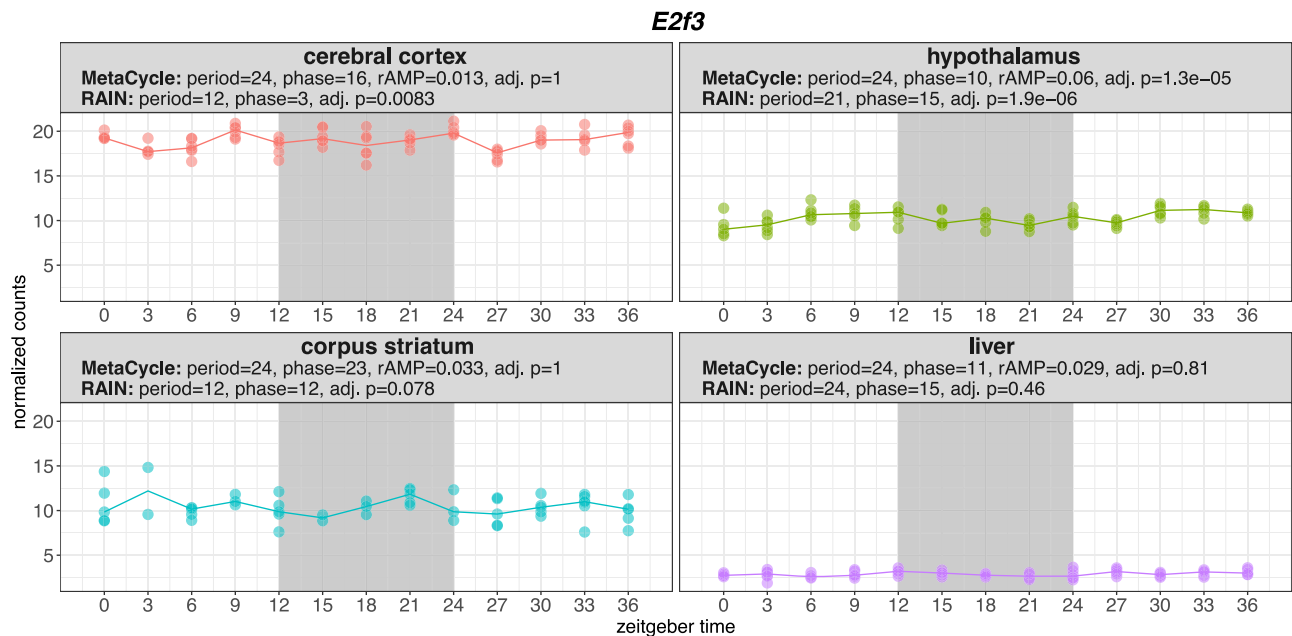


Fig. 3 | Expression and cycling parameters of the transcription factor gene *E2f3*. Sampling timepoints represented in Zeitgeber time are on the x-axis. Normalized gene expression counts are on the y-axis. Data points represent the normalized

counts of *E2f3* at each timepoint and tissue. Panel titles indicate the tissue, *MetaCycle* results, and *RAIN* results.

(Fig. 9a; Supplementary Data 13). Most modules appeared heterogeneous and contained gene markers for multiple cell types, including neurons and glial/immune cells, such as oligodendrocytes, microglia/perivascular macrophages, and astrocytes. The cortical *grey60* module specifically was enriched for oligodendrocyte, astrocyte, and endothelial cell markers and pathways, including myelination, glial cell differentiation, and oligodendrocyte differentiation (Fig. 9b, c; Supplementary Data 14). These results suggest that rhythmic cell-cell communication may play an important role in driving CNS biology.

Finally, we sought to detail the cell- and site-specific nature of cycling genes at the protein level and focused on the *grey60* module in the cortex, given its bias towards glial cell types and that ~80% of its genes were *RAIN* cycling genes ($P_{g,SCS} < 0.05$). The hub gene in this module, transferrin, showed rhythmic expression with a trough at ZT2 and a peak at ZT14 (Fig. 10a, b) and has previously been shown to be expressed by oligodendrocytes³³. IL-33, also in this module and known to play a role in myelination^{34,35}, displayed diurnal changes in immunofluorescent intensity in cortical Olig2+ cells that peaked at ZT14 (Fig. 10c, d; Supplementary Fig. 15a, b, 16a). These results align with recent data showing that oligodendrocyte precursor cell (OPC) dynamics are subject to time-of-day differences in the naïve cortex via *Bmal1*, regulating sleep architecture and OPC complexity³⁶. Candidate genes *Fzd4*, *Eif1b*, *Lrrk2*, *Sphk2*, and *Adipor2* were also selected for protein analysis given their strong rhythmicity and differing phases in the cortex and hypothalamus. We found these targets to be expressed rhythmically at the protein level in neurons across the CNS. *Adipor2* showed rhythmic expression in hypothalamic neurons (peaking at ZT14), while *Fz-4* expression peaked at ZT8 in cortical neurons (Supplementary Figs. 15a, c, d, 16b, c). *Eif1b*, on the other hand, exhibited rhythmic immunofluorescence in cortical neurons with increased expression at ZT20/2 and reduced expression at ZT8/14 (Supplementary Figs. 15a, e, 16d). *Sphk2* and *LRRK2* colocalized with neurons in the cortex but had no significant changes in fluorescence intensity across the timepoints examined (Supplementary Figs. 15a, f, g, 16e, f). These findings highlight the need for cataloging changes in rhythmic expression at both the gene- and protein-level, in a cell- and site-specific manner.

Discussion

We identify cycling mRNAs, miRNAs, gene networks, and mRNA–miRNA co-expression pairs in the naïve CNS, which were validated at the protein-level with cellular resolution. Importantly, these rhythmic changes were both tissue- and cell-specific, highlighting the different expression characteristics of cycling genes and their variability across CNS sites. Thus, diurnal rhythmicity must be considered when planning experiments assessing gene function/activity and behavioral outcomes, for which our curated catalog can be a starting point (<https://www.ghasemloulab.ca/chronocNS/>).

Our study confirms previous findings that diurnal gene expression is highly tissue-specific, especially since cycling genes shared across tissues may have different parameters (e.g., phase)⁷. Further, the known function of these genes is also tissue-specific. For example, cycling genes in the cortex are uniquely involved in synapse organization and axonogenesis. This result is striking since the study that found that 6% of the forebrain cortex's transcriptome is cycling also found that synaptic transcripts are under strong circadian control⁹. The same group also found more cycling synaptic proteins than synaptic transcripts, meaning rhythmicity was most likely set at the post-transcriptional stage. To our knowledge, this study is the first to identify putative miRNA–mRNA pairs that could explain this discrepancy. These results have important translational potential given that both circadian rhythms and miRNAs have roles in neurodegenerative diseases, in which synaptic plasticity is disrupted, such as Alzheimer's Disease and Parkinson's Disease^{37,38}. For instance, several studies now show the utility of circadian miRNAs (or *circaMiRs*) as biomarkers in both healthy and disease states^{39–41}.

We identified groups of co-expressed mRNAs and miRNAs using gene network analysis, many of which were over-represented by cycling genes, with some having signatures of neuronal and/or glial cells. For example, the cortical *grey60* module was only enriched in glial cell markers and gliogenesis pathways. In this module, *Il33* exhibited rhythmic protein expression in oligodendrocytes. Meanwhile, the hypothalamus-specific *saddlebrown* cluster was only enriched in neuronal markers, with *Adipor2* being rhythmic, particularly in neurons. These results confirm evidence from others that cycling gene expression is cell-specific^{42,43}, and further support evidence that both glia and neurons are under circadian control^{5,43}.

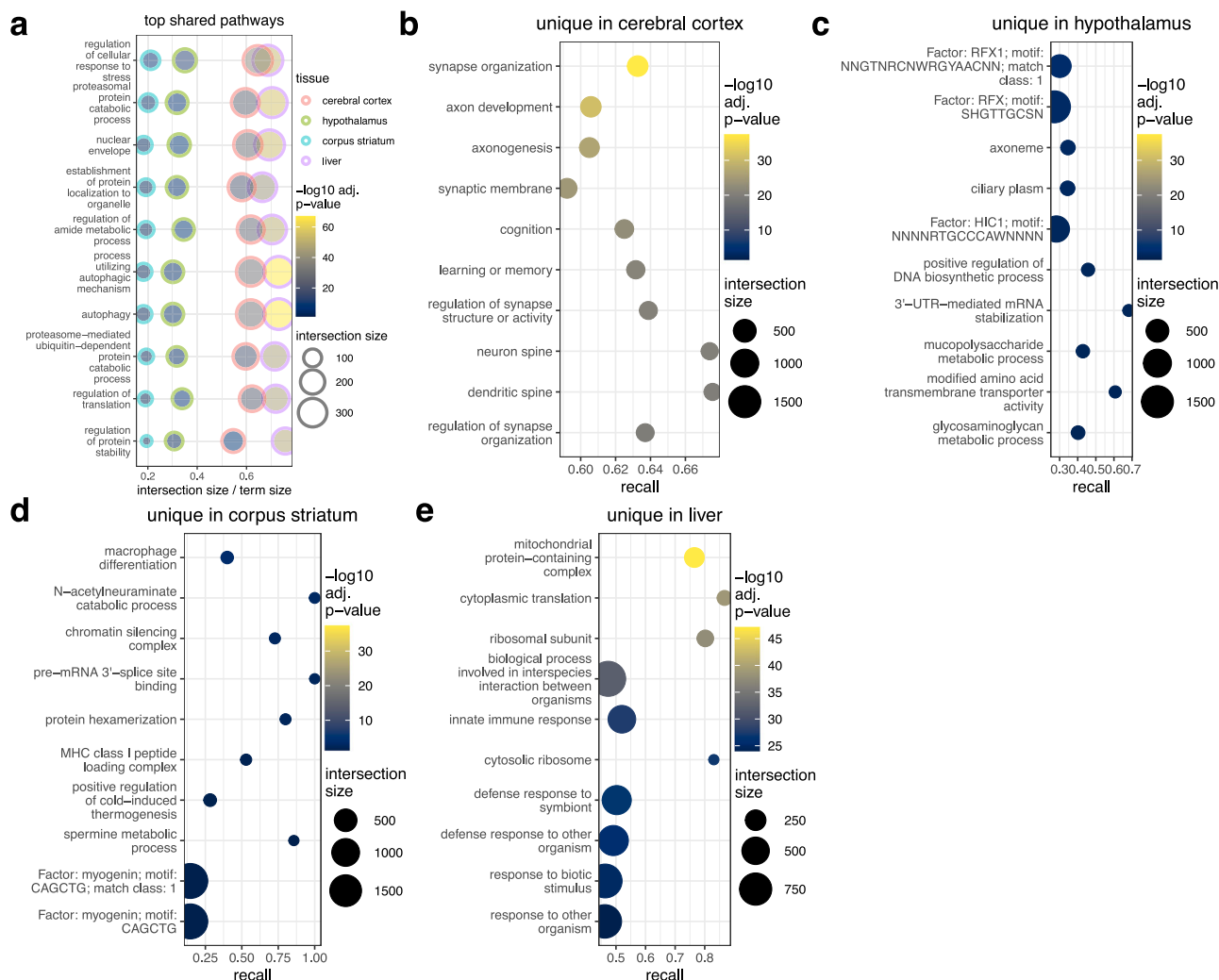


Fig. 4 | Comparison of pathways enriched in cycling genes across tissues. a Top pathways that are enriched in all 4 tissues ($P_{\text{g:SCS}} < 0.05$; $10 \leq \text{term size} \leq 500$). Intersection size is the number of genes that are both cycling and in a pathway. Recall

is the intersection size divided by the size of a term/pathway. **b–e** Top pathways uniquely enriched in their respective tissues ($P_{\text{g:SCS}} < 0.05$; $10 \leq \text{term size} \leq 500$).

Disruption of these rhythms likely contributes to clinical pathologies, including chronic pain, neurodegenerative and demyelinating diseases^{44,45}.

The transcriptomic rhythmicity of these sites has previously been described and, in addition to other tissues, can be explored using various databases, notably CircaDB⁴⁶, CGDB⁴⁷, and CircadiOmics⁴⁸. However, these databases either rely on microarrays and not the more robust RNA-sequencing, fail to account for site-specific rhythms, do not capture an adequate number of data points to account for ultra/infradian rhythms, and/or lack data on miRNAs. In addition, rhythms are likely governed at the cellular level. Single-cell circadian datasets of the CNS are only available for the murine suprachiasmatic nucleus and liver, and the much less complex *Drosophila* brain^{42,43,49}. A recent spatial cell type atlas of the mouse brain contains samples taken from both the light and dark phases⁵. While this dataset captured diurnal changes of clock genes, non-clock genes were not assessed. As such, more comprehensive databases using single-cell methods are necessary to fully capture the extent of rhythmicity at both site- and cellular-specific levels.

Despite our study providing important insights into the diurnal rhythmicity of gene expression and post-transcriptional regulation in the CNS, our study has limitations. Our study used a publicly available dataset that was created to identify diurnal gene expression patterns²⁵, but its characteristics may be optimized to better address this study's aims. First, the mice are 6-months-old compared to ~6–12-weeks-old mice previously

used to study circadian gene rhythmicity^{7,9,10,14,24}. Aging has been shown to reduce gene rhythmicity in mice^{50,51}; however, rhythmicity appears consistent between ~6-week-old mice and 6-month-old mice⁵¹, and this decrease in rhythmicity does not occur until later in life⁵¹. Second, this study only examines samples from male mice. While diurnal/circadian genome atlas studies have focused on male mice/primates^{7,26,42}, evidence suggests that circadian gene expression has sex-specificity^{52–55}. This male bias likely skews our understanding of female gene rhythmicity⁵⁶, and it is critical that female subjects are incorporated in future studies. Third, mice were entrained to a 12:12 light/dark cycle during sample collection, so cycling genes may be partially influenced by external stimuli such as light and food⁵⁷. Fourth, samples were collected over a 36-h period, but a 48-h period would be preferred. This shorter sampling period may be insufficient to show that rhythms with a period ≥ 18 -h repeat in their entirety. While we may show that genes with a 24-h period begin to repeat, including circadian clock genes having their expected 24-h periods, infradian genes particularly need to be confirmed with a longer sampling period. Finally, while we use immunohistochemistry to perform experimental validation of select cycling mRNAs, more extensive validation of cycling mRNAs, miRNAs, and their interactions in their tissue context needs to be performed.

To the best of our knowledge, we provide the first examination of mRNA and miRNA rhythmicity and their interactions in the mouse cortex, hypothalamus, and corpus striatum. Our work builds a foundation for the

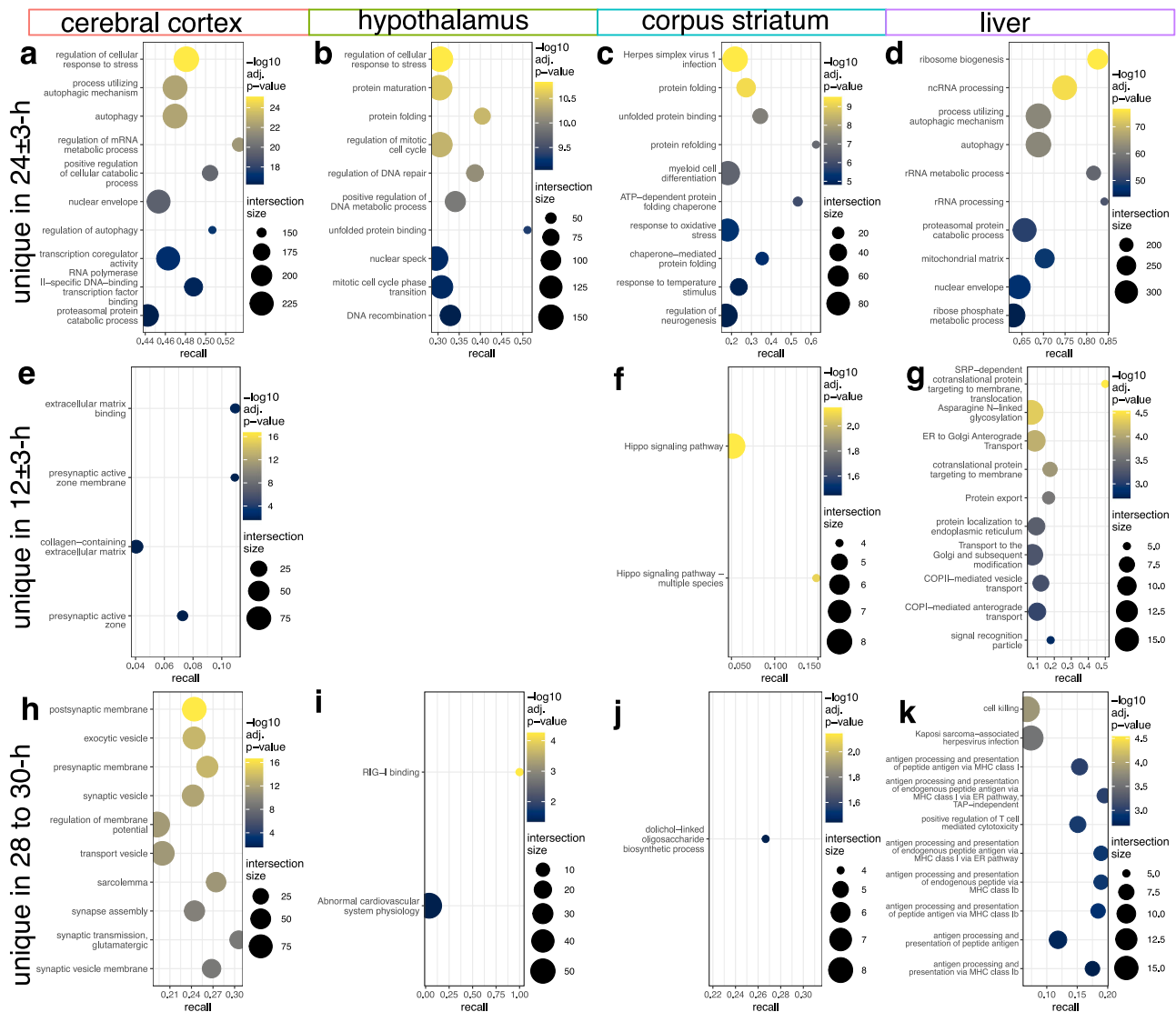


Fig. 5 | Comparison of pathways enriched in cycling mRNAs across period length categories (24-h, 12-h, and 28- to 30-h). Top pathways that are uniquely enriched in the three period categories for each tissue ($P_{\text{GSCS}} < 0.05$; $10 \leq \text{term size} \leq 500$). Intersection size is the number of genes that are both cycling and in a pathway. Recall is the intersection size divided by the size of a term/pathway.

study of circadian rhythms in the CNS by better understanding the naïve state, particularly given the contribution of identified cycling genes across neurological diseases, including Parkinson's^{58–60}, stroke⁶¹, and glioma^{62,63}, among others.

Methods

Transcriptomics analysis study design & data description

Our curated workflow for transcriptomics data analysis is summarized in Supplementary Fig. 1 and detailed below. We used *SRA-Toolkit* v2.10.8 to download data from Gene Expression Omnibus (GEO): GSE151567^{64,65}. As described by Wang et al.²⁵, wild-type C57BL/6J male were purchased from the Jackson Lab (JAX:000664). Mice aged 22 weeks were singly housed within circadian cabinets under a 12:12 light/dark cycle. At 26 weeks, the cerebral cortex, corpus striatum, hypothalamus, and liver of mice were harvested every 3-h for 36-h. At each timepoint, two mice were chosen pseudorandomly from different cabinets. Only mice that were active in the dark period and had been resting for >15 min in the light period were used. Time 0 represents the beginning of daylight, and 12 is the beginning of darkness. After tissues were harvested, they were flash-frozen and

a, e, h Comparison of pathways within the cerebral cortex. b, i Comparison of pathways within the hypothalamus. No pathways were unique to the period category 12 ± 3-h. For i, results are not filtered by term size. c, f, j Comparison of pathways within the corpus striatum. d, g, k Comparison of pathways within the liver.

transferred to Expression Analysis, Inc. for mRNA and miRNA extraction and sequencing. There were 2–6 biological replicates for each timepoint, with the exception that there were no miRNA-seq samples from Zeitgeber time 15 in the striatum (Supplementary Fig. 17a). Specifically, the following numbers of samples were used for mRNA-sequencing (mRNA-seq) analysis: (i) cortex: $n = 6/\text{timepoint}$; (ii) hypothalamus: $n = 6/\text{timepoint}$ except ZT9 $n = 5$; (iii) striatum: ZT0 = 5, ZT3 = 3, ZT6 = 5, ZT9 = 3, ZT12 = 6, ZT15 = 2, ZT18 = 4, ZT21 = 6, ZT24 = 4, ZT27 = 5, ZT30 = 6, ZT33 = 6, ZT36 = 5; (iv) liver: $n = 6/\text{timepoint}$ except ZT33 $n = 5$. The following number of samples were used for miRNA-seq analysis: (i) cortex: $n = 6/\text{timepoint}$, (ii) hypothalamus: ZT0, 6, 12, 24–36 $n = 6/\text{timepoint}$, ZT3, 15–21 $n = 5/\text{timepoint}$, ZT9 $n = 4$; (iii) striatum: ZT0 = 3, ZT3 = 3, ZT6 = 3, ZT9 = 4, ZT12 = 5, ZT15 = 0, ZT18 = 2, ZT21 = 5, ZT24 = 4, ZT27 = 3, ZT30 = 5, ZT33 = 5, ZT36 = 4; liver: $n = 6/\text{timepoint}$ except ZT33 $n = 5$.

Transcriptomics data preparation

We evaluated the quality of sequencing reads with *FastQC* v0.11.9 and *MultiQC* v1.12^{66,67}. For mRNA-seq reads, we filtered for base quality with *Trimmomatic* v0.36 and aligned reads to the mouse genome (GENCODE

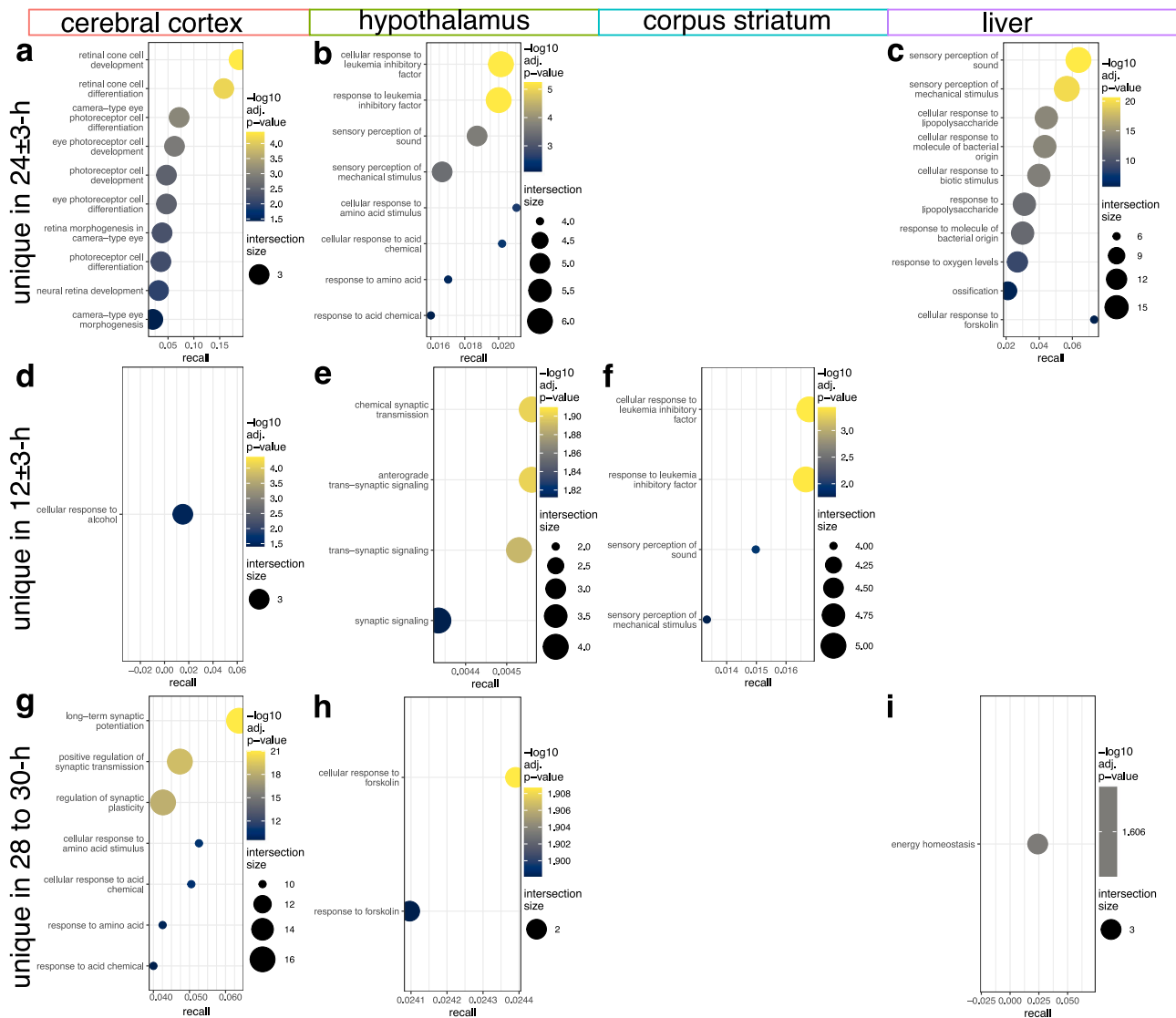


Fig. 6 | Comparison of pathways enriched in cycling miRNAs across period length categories (24-h, 12-h, and 28- to 30-h). Top pathways that are uniquely enriched in the 3 period categories for each tissue ($P_{\text{eSCS}} < 0.05$; $10 \leq \text{term size} \leq 500$). Intersection size is the number of genes that are both cycling and in a pathway. Recall is the intersection size divided by the size of a term/pathway.

a, d, g Comparison of pathways within the cerebral cortex. **b, e, h** Comparison of pathways within the hypothalamus. For **e**, results are not filtered by term size. **f** Comparison of pathways within the corpus striatum. No pathways were unique to the period category 24 \pm 3-h nor 28- to 30-h. **c, i** Comparison of pathways within the liver. No pathways were unique to the period category 12 \pm 3-h.

release M32) with *Hisat2* v2.2.1^{68–70}. Gene expression was quantified with *StringTie* v2.1.5, and R package *IsoformSwitchAnalyzeR* v1.18.0^{71,72}. Adapted from Rahmanian et al.⁷³ miRNA-seq processing pipeline, we removed 3' adapters from miRNA reads, filtered for base quality, aligned, and quantified gene expression using *CutAdapt* v4.2, *Trimomatic* v0.36, and *STAR* v2.7.9a^{68,74,75}. Overall and unique alignment rates were calculated to evaluate performance. One mRNA and one miRNA sample from the striatum were removed before quantification due to low overall alignment rates (35% and 34.66%, respectively; Supplementary Fig. 18).

With the generated gene count matrixes, we evaluated this experiment's technical variability by finding the Spearman correlation between samples from the same tissue and timepoint (Supplementary Fig. 19). Then, we performed outlier detection and TMM normalization using the R packages *arrayQualityMetrics* v3.60.0 and *edgeR* v4.2.0, respectively^{76,77}. *arrayQualityMetrics* uses three metrics to consider a sample an outlier: 1) its sum of distances to other samples, 2) the Kolmogorov-Smirnov statistic, and 3) the Hoeffding's *D*-statistic. Samples were removed if marked an outlier before and after normalization, or if multiple metrics marked them an

outlier after normalization. After removing outliers, we re-normalized gene counts, and outlier detection was repeated. Based on these metrics, we removed four (cortex), two (hypothalamus), five (striatum), and nine (liver) samples from the mRNA dataset. One striatum and one liver sample were removed from the miRNA dataset. We used principal component analysis on variance stabilizing transformed counts to visualize the clustering of samples with *DESeq2* v1.44.0 (Supplementary Fig. 20)⁷⁸. Two mRNA hypothalamus samples appeared to be outliers and were removed. The final study design is displayed in Supplementary Fig. 17b. Finally, we considered genes to be expressed for each tissue if their mean normalized counts per million were ≥ 1 . There were 18,444 (cortex), 18,712 (hypothalamus), 18,248 (striatum), and 13,514 (liver) mRNA genes remaining. For the miRNA dataset, there were 459 (cortex), 462 (hypothalamus), 458 (striatum), and 284 (liver) remaining miRNAs.

Identifying rhythmic features

Cycling mRNA and miRNAs were detected using R packages *MetaCycle* v1.2.0 and *RAIN* v1.38.0^{19,20}. For *MetaCycle*, we used the *meta2d* function

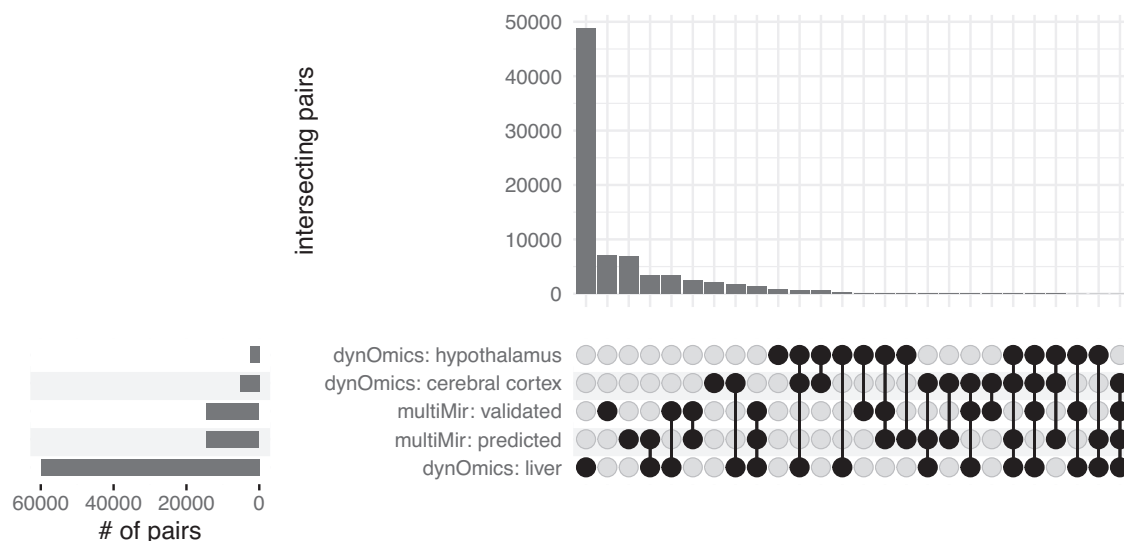


Fig. 7 | mRNA-miRNA association analysis. Intersections between mRNA-miRNA pairs associated ($P_{BH} < 0.05$) across tissues and previously reported pairs from *multiMir*.

with a minimum and maximum period of 24. *P*-values from the Lomb-Scargle and Jonckheere-Terpstra-Kendall cycle algorithms were combined with Fisher's method and corrected for multiple testing with the Benjamini-Hochberg method. For *RAIN*, we used the rain function with the parameters “period = 17”, “period.delta = 13”, and *RAIN*'s adaptive Benjamini-Hochberg multiple testing correction. *MetaCycle* was also used to run the *ARSER* algorithm. For *ARSER*, one replicate from each timepoint was randomly selected. We then used the meta2d function with the parameters “minper = 4”, “maxper = 30”, and “cycMethod = c(‘ARS’)”. For a gene with multiple cycles, the highest amplitude cycle was considered dominant and further analyzed. Cycling genes had an adjusted $P < 0.05$. Functional enrichment analysis of cyclic genes was performed with R package *gprofiler2* v0.2.3, with the g:SCS multiple testing correction method^{79,80}. The databases queried with *gprofiler2* included Gene Ontology^{81,82}, KEGG⁸³, Reactome⁸⁴, WikiPathways⁸⁵, TRANSFAC⁸⁶, miRTarBase⁸⁷, the Human Protein Atlas⁸⁸, CORUM⁸⁹, and Human Phenotype Ontology⁹⁰. Finally, we found the overlap between *MetaCycle* rhythmic genes and proximal/eQTL-mapped genes corresponding to 236 putative causal single-nucleotide polymorphisms that Jones et al.²⁸ previously associated with self-reported chronotype in humans. The statistical significance of overlaps was tested using hypergeometric tests, where significant overlaps would have had a Benjamini-Hochberg adjusted p -value < 0.05 . The background set for all hypergeometric tests was the genes remaining after nonspecific filtering.

Integrating mRNA and miRNA pairwise

To discover relationships between cycling mRNAs and miRNAs, we used R packages *lms* v1.3.3 and *dynOmics* v1.0 to collapse replicates and find the delayed Pearson correlations between cycling mRNA-miRNA pairs^{91,92}. After accounting for the predicted delay in log2 expression, significant associations had a $P_{BH} < 0.05$. We considered associations with a negative correlation and time delay ≤ 0 , i.e., decreased mRNA expression after miRNA expression, to be potential miRNA direct targets. These associations were compared to predicted and/or experimentally confirmed mRNA targets of cycling miRNAs identified with the R package *multiMir* v1.26.0⁹³. *MultiMir* compiles predicted miRNA-targets from the databases DIANA-microT-CDS⁹⁴, EIMMo⁹⁵, MicroCosm⁹⁶, miRanda⁹⁷, miRDB⁹⁸, PicTar⁹⁹, PITA¹⁰⁰, and TargetScan¹⁰¹. These resources used miRNA-mRNA sequence complementarity, mRNA-miRNA duplex thermodynamics, and/or species conservation to identify miRNA targets. Before querying these databases, the precursor miRNA IDs were converted to their respective mature versions with R package *miRBaseConverter* v1.11.1¹⁰².

Identifying co-expression networks of mRNA and miRNA

We used weighted gene co-expression network analysis (R package WGCNA v1.72-5) to find interactions between groups of co-expressed mRNA and miRNAs¹⁰³. We calculated the pairwise Pearson correlations between the log2-transformed gene counts for each tissue. We calculated gene similarities by adding 1 to each correlation and dividing by 2, thus creating a signed network. Using various soft-thresholding powers, we created weighted adjacency matrixes with scale-free topology fits ($R^2 > 0.8$. mRNA powers: 16 (cortex), 16 (hypothalamus), 18 (striatum), 16 (liver). miRNA powers: 4 (cortex), 5 (hypothalamus), 6 (striatum), and 9 (liver). We then calculated topological overlap matrices (TOM). Based on dissimilarity (1-TOM), genes were grouped into modules by hierarchical clustering with the dynamic tree-cut algorithm.

Once the networks were constructed, we found each module's hub gene, which is the gene with the highest connectivity within a module. We also used a hypergeometric test to determine the enrichment of cycling genes, both from *MetaCycle* and *RAIN*. We then used the Spearman correlation between mRNA and miRNA “cycling” modules' eigengenes to find potential mRNA-miRNA relationships, with *P*-values adjusted using the Benjamini-Hochberg method. We also used a hypergeometric test to determine the enrichment of brain cell types in cycling modules. Yao et al.¹⁰⁴ single-cell sequencing data from the mouse cortex and hippocampus provided the gene-expression profiles of cell types. For each cell type cluster ($n = 387$), we considered a marker gene identified by Yao et al.¹⁰⁴ to be expressed if its trimmed mean expression is greater than zero. We then found the overlap between genes expressed in a cell type cluster and a module. For visualization, cell type clusters were collapsed into higher-level neighborhoods (MGE, DR/SUB/CA, CGE, L2/3 IT, L4/5/6 IT Car 3, NP/CT/L6b, PT, and Other). Cell types in the “Other” neighborhood are instead collapsed into their respective subclasses (Meis2, Oligo, CR, Astro, SMC-Peri, Micro-PVM, Endo, and VLMC). The grey60 module in the cortex was visualized with *Cytoscape* 3.10.0¹⁰⁵. Finally, we performed pathway analysis of modules with R package *gprofiler2*, as described above.

Animals for immunohistochemistry

All work was performed using 20- to 30-week-old C57BL/6J male mice, matching the animals' age in the miRNA/mRNA-seq datasets. The institutional animal care and use committees of Queen's University approved all animal care and procedures (Protocol # 2023-2428) following all guidelines of the Canadian Council on Animal Care. We have complied with all relevant ethical regulations for animal use.

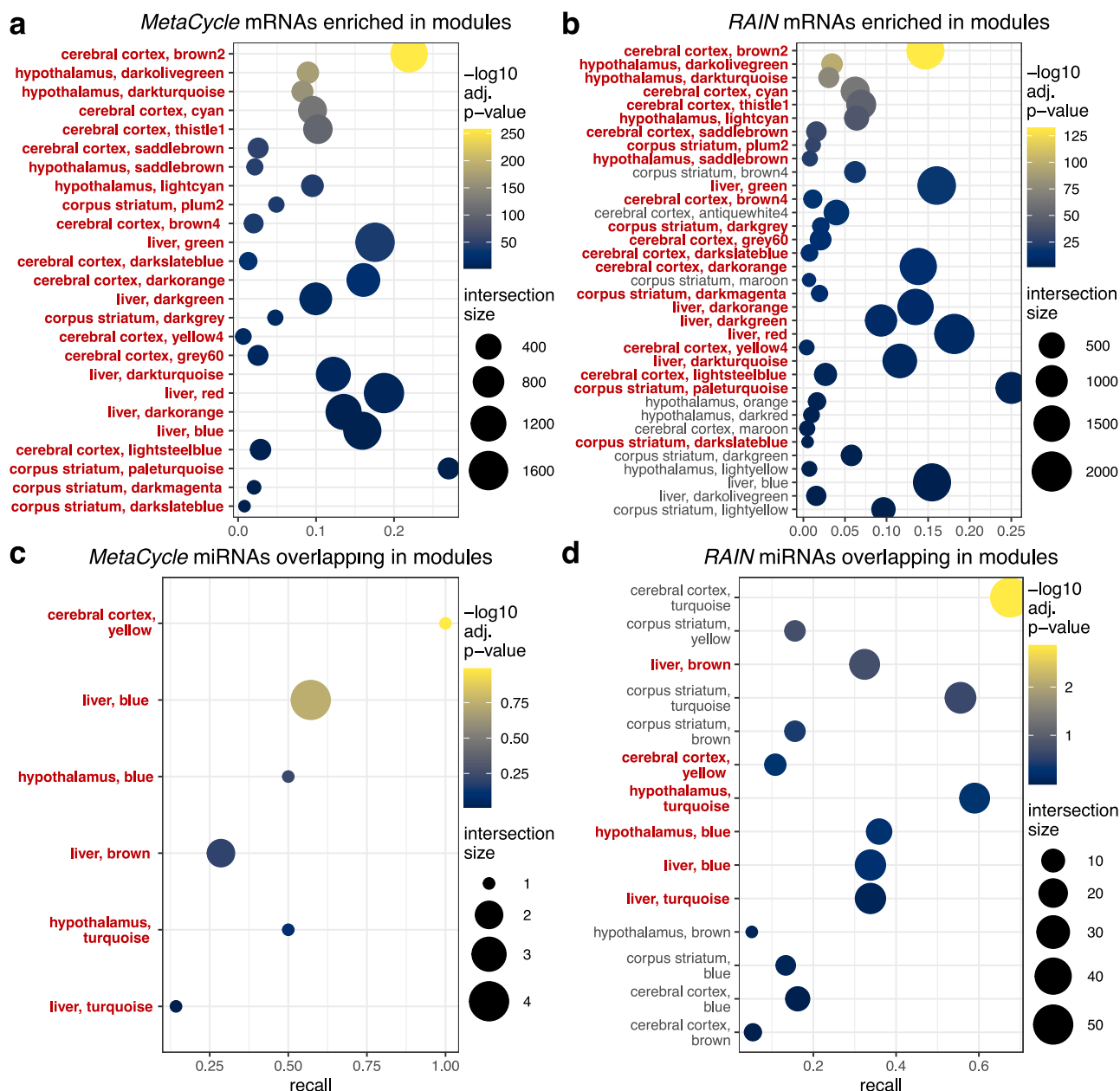


Fig. 8 | Network analysis and enrichment of cycling genes. Overlap between gene modules and cycling genes. Intersection size is the number of genes that are both cycling and in a module. Recall is the intersection size divided by the total number of cycling genes considered. Datapoints are colored by the $-\log_{10}(P_{\text{BH}})$ of cycling gene enrichment in a module. **a, b** mRNA modules enriched with cycling genes

($P_{\text{BH}} < 0.05$). **c, d** miRNA modules that contain at least one cycling gene. **a, c** Analysis of *MetaCycle* cycling genes in modules. **b, d** Analysis of *RAIN* cycling genes in modules. Modules that occur in both *MetaCycle* and *RAIN* results are emphasized by bold red text.

Immunohistochemistry

Animals were transcardially perfused with phosphate-buffered saline (PBS), followed by 4% paraformaldehyde. The brain was removed and placed into 30% sucrose in PBS for 24-h, embedded in Tissue TEK OCT (Fisher Scientific) and frozen at -80°C . 16 μm sections were collected using a Leica CM1950 cryostat (Leica). Sections were blocked with 4% BSA (Sigma-Aldrich) and 0.3% Triton X-100 (BioShop) in PBS for 1-h at room temperature and incubated overnight at 4°C with primary antibodies. Primary antibodies for proteins of interest were anti-IL-33 (1:50, cat.no.AF3626, R&D Systems), anti-AdipoR2 (1:200, cat.no. BS-0611R, Bioss), anti-FZD4 (1:200, cat.no. SAB4503265, Sigma-Aldrich), anti-EIF1B (1:100, cat.no. ABX326521, Abcam), anti-LRRK2 (1:200, cat.no.ab133474, Abcam), anti-SPHK2 (1:200, cat.no.17096-1-AP, Proteintech), and anti-Transferrin (1:50, cat.no. ZRB1225, Sigma-Aldrich). For markers of neurons, microglia,

astrocytes, and oligodendrocytes, anti-NeuN (1:200, cat.no MAB377, Sigma-Aldrich), anti-Iba1 (1:500, cat.no. 019-19741, Wako; 1:500 cat.no. 234 009, Synaptic Systems), anti-GFAP (1:1000, cat.no. 13-0300, Invitrogen; 1:1000), anti-Olig2 (1:250, cat.no. MABN50, Sigma Aldrich). After washing, sections were incubated with either Alexa Fluor 488, 594, or 647 conjugated secondary antibodies (1:500, Invitrogen) overnight at 4°C . Secondary antibody-only controls were used to confirm the specificity of primary antibodies (Supplementary Fig. 21). The slides were mounted using Prolong[™] Diamond Antifade Mountant with DAPI (Life Technologies). Randomization was not necessary and thus not performed.

Image analysis

Images were captured using an Eclipse Ti2 microscope (Nikon) with NIS-Elements AR (Nikon). Five $\times 40$ images were captured in the brain region

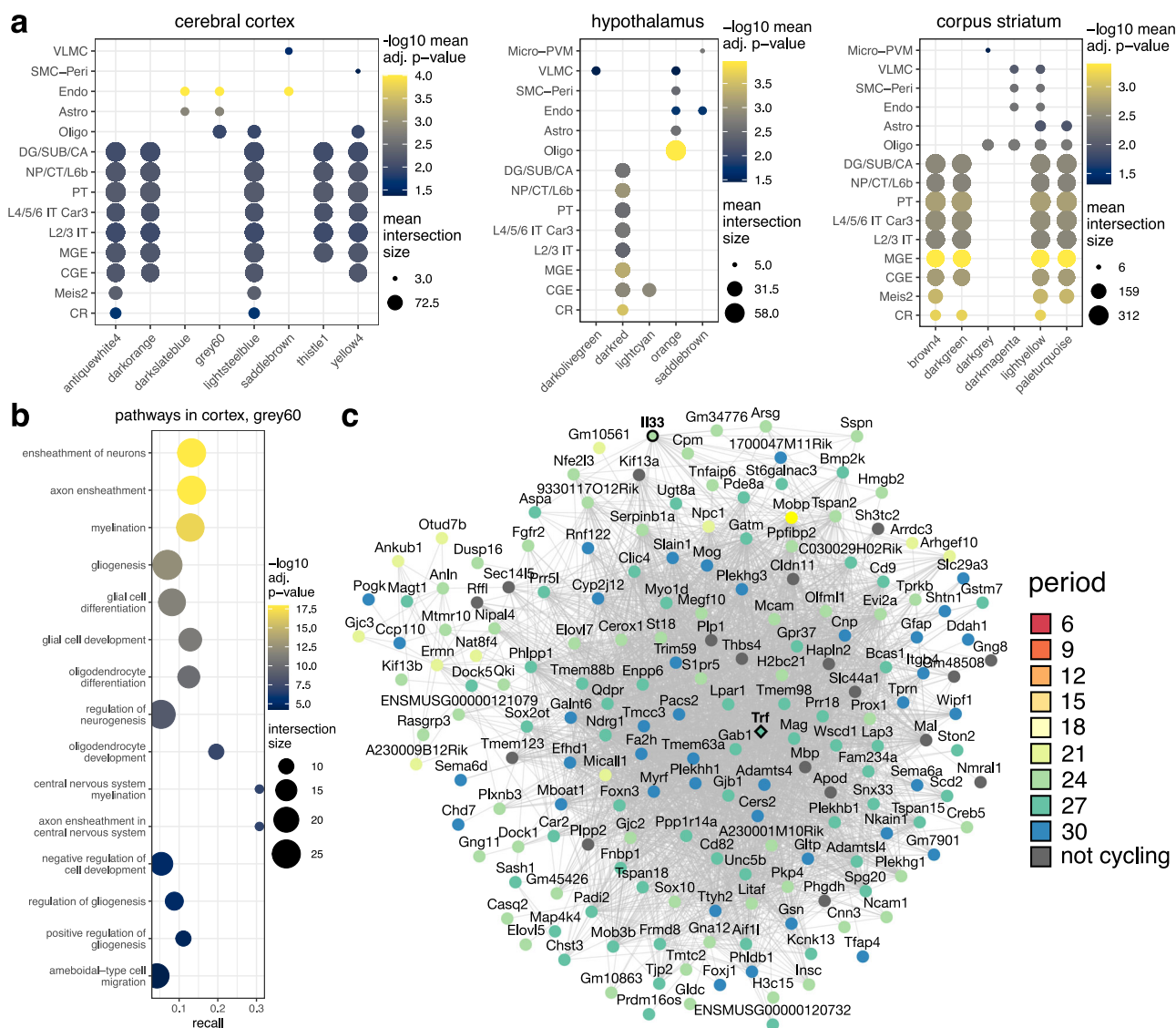


Fig. 9 | Enrichment of cell-type marker genes in cycling mRNA modules. **a** Cell type clusters ($n = 387$) are collapsed into previously defined neighborhoods (MGE, DR/SUB/CA, CGE, L2/3 IT, L4/5/6 IT Car 3, NP/CT/L6b, PT, and Other). The “Other” neighborhood clusters were collapsed into their respective subclasses (Meis2, Oligo, CR, Astro, SMC-Peri, Micro-PVM, Endo, and VLMC). *RAIN* cycling mRNA modules enriched in cell-type marker genes and their respective cell-type subclasses are shown ($P_{BH} < 0.05$). The size of datapoints represents the mean number of genes that are both a cell subclass marker gene and in a module, i.e., mean

intersection size. Datapoints are colored by the mean $-\log_{10}(P_{PH})$ of a cell type subclass’s marker genes enrichment in a cycling module. **b** Pathways enriched in the cortical grey60 module ($P_{gSCS} < 0.05$; $10 \leq \text{term size} \leq 500$). **c** mRNAs with an adjacency ≥ 0.03 are visualized ($n = 180$ of 290). mRNAs (circle nodes) are arranged based on co-expression adjacency (grey edges). Nodes of cycling genes are colored by period category. If a gene is not cycling, its node is colored grey. The hub gene has a diamond node. Genes that underwent immunohistochemistry analysis, *Trf* and *Il33*, have their nodes outlined in black and labels bolded.

of interest (ROI) for each animal, and for each protein and CNS cell marker staining combination. ImageJ (NIH) was used to quantify the fluorescence intensity of each protein within the boundaries of each CNS cell body. Multichannel images were split into single channels, and then channels containing CNS cell markers were thresholded to only contain fluorescence signals within the cell body. The thresholded image was turned into a selection, which created a ROI around the cells. The channel containing the target protein was converted to a 16 bit image so that pixel ranges were consistent, and the mean gray value of the image was measured. Then, the ROI’s were superimposed onto the channel, and the mean gray value of the ROI was measured. A circular ROI with a diameter of $20 \mu\text{m}$ (area $316.204 \mu\text{m}^2$) was created and placed in a region of the image without target protein signal to measure background fluorescence. To calculate fluorescence intensity, the mean background fluorescence was subtracted from the mean fluorescence intensity of the CNS cell ROI.

The fluorescence intensity for each image was averaged together. The immunohistochemistry investigator needed to know the site and time point for data collection, but they were blinded to the time of data collection for analysis.

Statistics and reproducibility

Unless otherwise described, transcriptomics data analyses were conducted in R v4.4.0¹⁰⁶. Immunohistochemistry analyses used Graphpad Prism (v10, Graphpad Software, Boston, USA). Analysis of variance (ANOVA) was used to compare protein fluorescence data across timepoints and cell types, with significance thresholds set at $P < 0.05$, using the post hoc Tukey test and Holm-Sidak multiple comparisons test. As described above, transcriptomics had 2–6 mice per timepoint and tissue, except for zero miRNA-seq samples from ZT15 in the corpus striatum (Supplementary Fig. 17). Immunohistochemistry had four mice per timepoint and tissue.

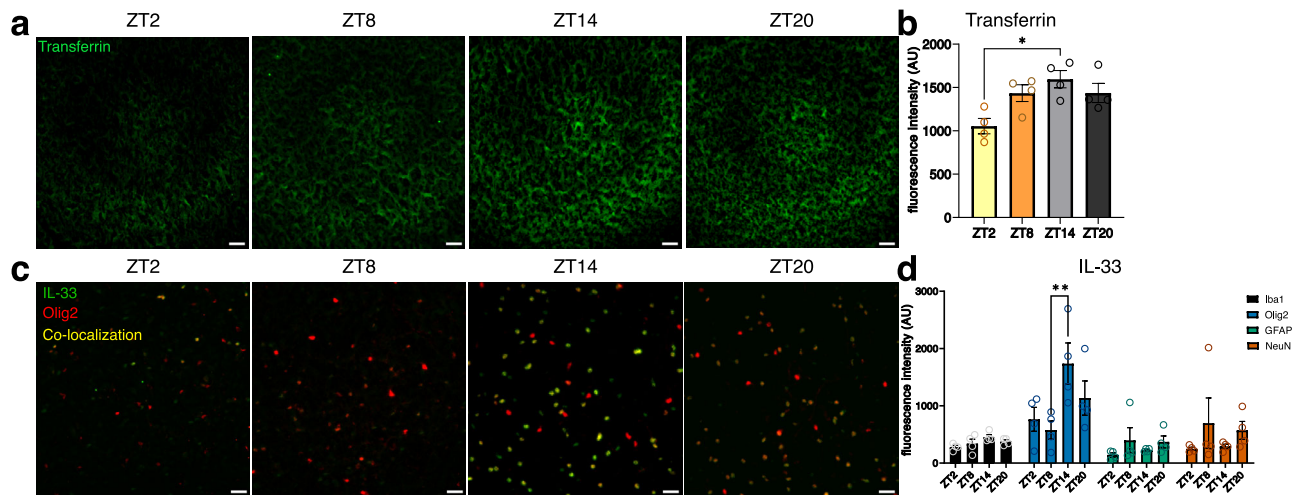


Fig. 10 | Rhythmic expression of extracellular transferrin and oligodendrocyte-specific IL-33 in the naïve CNS. **a** Representative images of transferrin staining in the cortex of brains collected at ZT2, ZT8, ZT14, and ZT20. Scale bar, 25 μ m. **b** Quantification of fluorescence intensity of the transferrin signal in the cortex. One-way ANOVA with Tukey's post hoc test, $n = 4$ animals for each timepoint. Transferrin ZT2 versus ZT14, $*P = 0.0106$, $q = 5.457$, d.f. = 12. **c** Representative images of cortical oligodendrocytes (labeled with Olig2), IL-33, and their co-localization at

ZT2, ZT8, ZT14, and ZT20. Scale bar, 25 μ m. **d** Quantification of fluorescence intensity of IL-33 signal co-localized in the cortex with Iba1 (microglia), Olig2 (oligodendrocyte marker), GFAP (astrocytes), and NeuN (neurons). Two-way ANOVA, with Tukey's post hoc test, $n = 4$ animals for each timepoint. IL-33 with Olig2, ZT8 versus ZT14, $**P = 0.0070$, $q = 6.093$, d.f. = 48. All data presented as mean \pm s.e.m.

Reporting summary

Further information on research design is available in the Nature Portfolio Reporting Summary linked to this article.

Data availability

Bulk sequencing data are available at [GSE151567](https://www.gse151567). Cycling genes and mRNA-miRNA pairs can be interactively explored at <https://www.ghasemloulab.ca/chronoCNS>. All other data supporting this study's findings are available from the corresponding authors upon reasonable request.

Code availability

No custom code was used to generate or process the data. However, scripts used to analyze data and generate figures are available at <https://github.com/ComputationalGenomicsLaboratory/chronoCNS>.

Received: 22 April 2025; Accepted: 10 June 2025;

Published online: 01 July 2025

References

- Fagiani, F. et al. Molecular regulations of circadian rhythm and implications for physiology and diseases. *Signal Transduct. Target. Ther.* **7**, 41 (2022).
- Jones, J. R., Chaturvedi, S., Granados-Fuentes, D. & Herzog, E. D. Circadian neurons in the paraventricular nucleus entrain and sustain daily rhythms in glucocorticoids. *Nat. Commun.* **12**, 5763 (2021).
- Smarr, B. L., Jennings, K. J., Driscoll, J. R. & Kriegsfeld, L. J. A time to remember: the role of circadian clocks in learning and memory. *Behav. Neurosci.* **128**, 283–303 (2014).
- de Zavalía, N. et al. Bmal1 in the striatum influences alcohol intake in a sexually dimorphic manner. *Commun. Biol.* **4**, 1227 (2021).
- Yao, Z. et al. A high-resolution transcriptomic and spatial atlas of cell types in the whole mouse brain. *Nature* **624**, 317–332 (2023).
- Coskun, A., Zarepour, A. & Zarrabi, A. Physiological rhythms and biological variation of biomolecules: the road to personalized laboratory medicine. *Int. J. Mol. Sci.* **24**, 6275 (2023).
- Zhang, R., Lahens, N. F., Ballance, H. I., Hughes, M. E. & Hogenesch, J. B. A circadian gene expression atlas in mammals: implications for biology and medicine. *Proc. Natl. Acad. Sci. USA* **111**, 16219–16224 (2014).
- Brami-Cherrier, K. et al. Cocaine-mediated circadian reprogramming in the striatum through dopamine D2R and PPAR γ activation. *Nat. Commun.* **11**, 4448 (2020).
- Noya, S. B. et al. The forebrain synaptic transcriptome is organized by clocks but its proteome is driven by sleep. *Science* **366**, eaav2642 (2019).
- Hughes, M. E. et al. Harmonics of circadian gene transcription in mammals. *PLoS Genet.* **5**, e1000442 (2009).
- Scott, M. R. et al. Twelve-hour rhythms in transcript expression within the human dorsolateral prefrontal cortex are altered in schizophrenia. *PLoS Biol.* **21**, e3001688 (2023).
- Reddy, A. B. et al. Circadian orchestration of the hepatic proteome. *Curr. Biol.* **16**, 1107–1115 (2006).
- Davis, G. M., Haas, M. A. & Pocock, R. MicroRNAs: not “fine-tuners” but key regulators of neuronal development and function. *Front. Neurol.* **6**, 245 (2015).
- Na, Y.-J. et al. Comprehensive analysis of microRNA-mRNA co-expression in circadian rhythm. *Exp. Mol. Med.* **41**, 638 (2009).
- Su, A. I. et al. A gene atlas of the mouse and human protein-encoding transcriptomes. *Proc. Natl. Acad. Sci. USA* **101**, 6062–6067 (2004).
- Du, N.-H., Arpat, A. B., De Matos, M. & Gatfield, D. MicroRNAs shape circadian hepatic gene expression on a transcriptome-wide scale. *Elife* **3**, e02510 (2014).
- Liang, Y., Ridzon, D., Wong, L. & Chen, C. Characterization of microRNA expression profiles in normal human tissues. *BMC Genom.* **8**, 166 (2007).
- Mei, W. et al. Genome-wide circadian rhythm detection methods: systematic evaluations and practical guidelines. *Brief. Bioinform.* **22**, bbaa135 (2021).
- Wu, G., Anafi, R. C., Hughes, M. E., Kornacker, K. & Hogenesch, J. B. MetaCycle: an integrated R package to evaluate periodicity in large scale data. *Bioinformatics* **32**, 3351–3353 (2016).
- Thaben, P. F. & Westermark, P. O. Detecting rhythms in time series with RAIN. *J. Biol. Rhythms* **29**, 391–400 (2014).
- Yang, R. & Su, Z. Analyzing circadian expression data by harmonic regression based on autoregressive spectral estimation. *Bioinformatics* **26**, i168–i174 (2010).
- Liao, M. et al. The P-loop NTPase RUVBL2 is a conserved clock component across eukaryotes. *Nature* **642**, 165–173 (2025).

23. Vollmers, C. et al. Circadian oscillations of protein-coding and regulatory RNAs in a highly dynamic mammalian liver epigenome. *Cell Metab.* **16**, 833–845 (2012).
24. Wang, H. et al. Oscillating primary transcripts harbor miRNAs with circadian functions. *Sci. Rep.* **6**, 21598 (2016).
25. Wang, N. et al. Mapping brain gene coexpression in daytime transcriptomes unveils diurnal molecular networks and deciphers perturbation gene signatures. *Neuron* **110**, 3318–3338.e3319 (2022).
26. Mure, L. S. et al. Diurnal transcriptome atlas of a primate across major neural and peripheral tissues. *Science* **359**. <https://doi.org/10.1126/science.aao0318> (2018).
27. Chan, A. B., Huber, A. L. & Lamia, K. A. Cryptochromes modulate E2F family transcription factors. *Sci. Rep.* **10**, 4077 (2020).
28. Jones, S. E. et al. Genome-wide association analyses of chronotype in 697,828 individuals provides insights into circadian rhythms. *Nat. Commun.* **10**, 343 (2019).
29. Wicht, H. et al. Chronotypes and rhythm stability in mice. *Chronobiol. Int.* **31**, 27–36 (2014).
30. Pfeffer, M., Wicht, H., von Gall, C. & Korf, H. W. Owls and larks in mice. *Front. Neurol.* **6**, 101 (2015).
31. Pfeffer, M., Korf, H.-W. & Wicht, H. The role of the melatoninergic system in light-entrained behavior of mice. *Int. J. Mol. Sci.* **18**, 530 (2017).
32. Pan, Y. et al. 12-h clock regulation of genetic information flow by XBP1s. *PLoS Biol.* **18**, e3000580 (2020).
33. Elkjaer, M. L. et al. Single-cell multi-omics map of cell type-specific mechanistic drivers of multiple sclerosis lesions. *Neurol. Neuroimmunol. Neuroinflamm.* **11**, e200213 (2024).
34. Allan, D. et al. Role of IL-33 and ST2 signalling pathway in multiple sclerosis: expression by oligodendrocytes and inhibition of myelination in central nervous system. *Acta Neuropathol. Commun.* **4**, 75 (2016).
35. Zarpelon, A. C. et al. Spinal cord oligodendrocyte-derived alarmin IL-33 mediates neuropathic pain. *FASEB J.* **30**, 54–65 (2016).
36. Rojo, D. et al. BMAL1 loss in oligodendroglia contributes to abnormal myelination and sleep. *Neuron* **111**, 3604–3618.e3611 (2023).
37. Videnovic, A., Lazar, A. S., Barker, R. A. & Overeem, S. The clocks that time us'—circadian rhythms in neurodegenerative disorders. *Nat. Rev. Neurol.* **10**, 683–693 (2014).
38. Li, S., Lei, Z. & Sun, T. The role of microRNAs in neurodegenerative diseases: a review. *Cell Biol. Toxicol.* **39**, 53–83 (2023).
39. Hicks, S. D. et al. Diurnal oscillations in human salivary microRNA and microbial transcription: implications for human health and disease. *PLoS ONE* **13**, e0198288 (2018).
40. Fawcett, S. et al. A time to heal: microRNA and circadian dynamics in cutaneous wound repair. *Clin. Sci.* **136**, 579–597 (2022).
41. Minhas, G. et al. Hypoxia in CNS pathologies: emerging Role of miRNA-based neurotherapeutics and yoga based alternative therapies. *Front. Neurosci.* **11**, 386 (2017).
42. Wen, S. A. et al. Spatiotemporal single-cell analysis of gene expression in the mouse suprachiasmatic nucleus. *Nat. Neurosci.* **23**, 456–467 (2020).
43. Dopp, J. et al. Single-cell transcriptomics reveals that glial cells integrate homeostatic and circadian processes to drive sleep–wake cycles. *Nat. Neurosci.* **27**, 359–372 (2024).
44. Brécier, A., Li, V. W., Smith, C. S., Halievski, K. & Ghasemlou, N. Circadian rhythms and glial cells of the central nervous system. *Biol. Rev. Camb. Philos. Soc.* **98**, 520–539 (2023).
45. Logan, R. W. & McClung, C. A. Rhythms of life: circadian disruption and brain disorders across the lifespan. *Nat. Rev. Neurosci.* **20**, 49–65 (2019).
46. Pizarro, A., Hayer, K., Lahens, N. F. & Hogenesch, J. B. CircaDB: a database of mammalian circadian gene expression profiles. *Nucleic Acids Res.* **41**, D1009–D1013 (2013).
47. Li, S. et al. CGDB: a database of circadian genes in eukaryotes. *Nucleic Acids Res.* **45**, D397–d403 (2017).
48. Samad, M., Agostinelli, F., Sato, T., Shimaji, K. & Baldi, P. CircadiOmics: circadian omic web portal. *Nucleic Acids Res.* **50**, W183–W190 (2022).
49. Droin, C. et al. Space-time logic of liver gene expression at sub-lobular scale. *Nat. Metab.* **3**, 43–58 (2021).
50. Welz, P.-S. & Benitah, S. A. Molecular connections between circadian clocks and aging. *J. Mol. Biol.* **432**, 3661–3679 (2020).
51. Wolff, C. A. et al. Defining the age-dependent and tissue-specific circadian transcriptome in male mice. *Cell Rep.* **42**, 111982 (2023).
52. Weger, B. D. et al. The mouse microbiome is required for sex-specific diurnal rhythms of gene expression and metabolism. *Cell Metab.* **29**, 362–382.e368 (2019).
53. Martini, T. et al. A sexually dimorphic hepatic cycle of periportal VLDL generation and subsequent pericentral VLDL-mediated re-uptake. *Nat. Commun.* **15**, 8422 (2024).
54. Astafev, A. A., Mezhnina, V., Poe, A., Jiang, P. & Kondratov, R. V. Sexual dimorphism of circadian liver transcriptome. *iScience* **27**, 109483 (2024).
55. van Rosmalen, L. et al. Multi-organ transcriptome atlas of a mouse model of relative energy deficiency in sport. *Cell Metab.* **36**, 2015–2037.e2016 (2024).
56. Walton, J. C., Bumgarner, J. R. & Nelson, R. J. Sex differences in circadian rhythms. *Cold Spring Harb. Perspect. Biol.* **14**. <https://doi.org/10.1101/cshperspect.a039107> (2022).
57. Hughes, M. E. et al. Guidelines for genome-scale analysis of biological rhythms. *J. Biol. Rhythms* **32**, 380–393 (2017).
58. Li, J.-Q., Tan, L. & Yu, J.-T. The role of the LRRK2 gene in Parkinsonism. *Mol. Neurodegener.* **9**, 47 (2014).
59. Ruiz, M. et al. Aging AdipoR2-deficient mice are hyperactive with enlarged brains excessively rich in saturated fatty acids. *FASEB J.* **38**, e23815 (2024).
60. Sugata, M., Kataoka, H. & Sugie, K. Association between adiponectin and lipids in Parkinson's disease. *Clin. Neurol. Neurosurg.* **254**, 108919 (2025).
61. Gasbarrino, K. et al. Decreased adiponectin-mediated signaling through the AdipoR2 pathway is associated with carotid plaque instability. *Stroke* **48**, 915–924 (2017).
62. De Boeck, A. et al. Glioma-derived IL-33 orchestrates an inflammatory brain tumor microenvironment that accelerates glioma progression. *Nat. Commun.* **11**, 4997 (2020).
63. Liu, J. et al. SPHK2 protein expression, Ki-67 index and infiltration of tumor-associated macrophages (TAMs) in human glioma. *Histol. Histopathol.* **33**, 987–994 (2018).
64. Leinonen, R., Sugawara, H. & Shumway, M. The sequence read archive. *Nucleic Acids Res.* **39**, D19–D21 (2011).
65. Edgar, R., Domrachev, M. & Lash, A. E. Gene Expression Omnibus: NCBI gene expression and hybridization array data repository. *Nucleic Acids Res.* **30**, 207–210 (2002).
66. Andrews, S. FastQC: A Quality Control Tool for High Throughput Sequence Data <http://www.bioinformatics.babraham.ac.uk/projects/fastqc/> (2015).
67. Ewels, P., Magnusson, M., Lundin, S. & Käller, M. MultiQC: summarize analysis results for multiple tools and samples in a single report. *Bioinformatics* **32**, 3047–3048 (2016).
68. Bolger, A. M., Lohse, M. & Usadel, B. Trimmomatic: a flexible trimmer for Illumina sequence data. *Bioinformatics* **30**, 2114–2120 (2014).
69. Frankish, A. et al. GENCODE 2021. *Nucleic Acids Res.* **49**, D916–d923 (2021).
70. Kim, D., Paggi, J. M., Park, C., Bennett, C. & Salzberg, S. L. Graph-based genome alignment and genotyping with HISAT2 and HISAT-genotype. *Nat. Biotechnol.* **37**, 907–915 (2019).

71. Pertea, M. et al. StringTie enables improved reconstruction of a transcriptome from RNA-seq reads. *Nat. Biotechnol.* **33**, 290–295 (2015).
72. Vitting-Seerup, K. & Sandelin, A. IsoformSwitchAnalyzeR: analysis of changes in genome-wide patterns of alternative splicing and its functional consequences. *Bioinformatics* **35**, 4469–4471 (2019).
73. Rahmiani, S. et al. Dynamics of microRNA expression during mouse prenatal development. *Genome Res.* **29**, 1900–1909 (2019).
74. Martin, M. Cutadapt removes adapter sequences from high-throughput sequencing reads. *EMBnet J.* **17**, 3 (2011).
75. Dobin, A. et al. STAR: ultrafast universal RNA-seq aligner. *Bioinformatics* **29**, 15–21 (2013).
76. Kauffmann, A., Gentleman, R. & Huber, W. arrayQualityMetrics—a bioconductor package for quality assessment of microarray data. *Bioinformatics* **25**, 415–416 (2009).
77. Robinson, M. D., McCarthy, D. J. & Smyth, G. K. edgeR: a Bioconductor package for differential expression analysis of digital gene expression data. *Bioinformatics* **26**, 139–140 (2010).
78. Love, M. I., Huber, W. & Anders, S. Moderated estimation of fold change and dispersion for RNA-seq data with DESeq2. *Genome Biol.* **15**, 550 (2014).
79. Raudvere, U. et al. g:Profiler: a web server for functional enrichment analysis and conversions of gene lists (2019 update). *Nucleic Acids Res.* **47**, W191–W198 (2019).
80. Kolberg, L., Raudvere, U., Kuzmin, I., Vilo, J. & Peterson, H. gprofiler2 -- an R package for gene list functional enrichment analysis and namespace conversion toolset g:Profiler. *F1000Res.* **9**. <https://doi.org/10.12688/f1000research.24956.2> (2020).
81. Ashburner, M. et al. Gene ontology: tool for the unification of biology. *Nat. Genet.* **25**, 25–29 (2000).
82. Gene Ontology Consortium. The Gene Ontology knowledgebase in 2023. *Genetics* **224** <https://doi.org/10.1093/genetics/iyad031> (2023).
83. Kanehisa, M., Furumichi, M., Sato, Y., Matsuura, Y. & Ishiguro-Watanabe, M. KEGG: biological systems database as a model of the real world. *Nucleic Acids Res.* **53**, D672–D677 (2024).
84. Milacic, M. et al. The Reactome Pathway Knowledgebase 2024. *Nucleic Acids Res.* **52**, D672–D678 (2023).
85. Agrawal, A. et al. WikiPathways 2024: next generation pathway database. *Nucleic Acids Res.* **52**, D679–D689 (2023).
86. Matys, V. et al. TRANSFAC and its module TRANSCompel: transcriptional gene regulation in eukaryotes. *Nucleic Acids Res.* **34**, D108–D110 (2006).
87. Huang, H. Y. et al. miRTarBase update 2022: an informative resource for experimentally validated miRNA–target interactions. *Nucleic Acids Res.* **50**, D222–d230 (2022).
88. Uhlén, M. et al. Tissue-based map of the human proteome. *Science* **347**, 1260419 (2015).
89. Tsitsiridis, G. et al. CORUM: the comprehensive resource of mammalian protein complexes–2022. *Nucleic Acids Res.* **51**, D539–D545 (2022).
90. Gargano, M. A. et al. The Human Phenotype Ontology in 2024: phenotypes around the world. *Nucleic Acids Res.* **52**, D1333–d1346 (2024).
91. Straube, J., Gorse, A. D., Team, P. C.oE., Huang, B. E. & Le Cao, K. A. A linear mixed model spline framework for analysing time course ‘Omics’ data. *PLoS ONE* **10**, e0134540 (2015).
92. Straube, J., Huang, B. E. & Cao, K. L. DynOmics to identify delays and co-expression patterns across time course experiments. *Sci. Rep.* **7**, 40131 (2017).
93. Ru, Y. et al. The multiMiR R package and database: integration of microRNA–target interactions along with their disease and drug associations. *Nucleic Acids Res.* **42**, e133 (2014).
94. Tastsoglou, S. et al. DIANA–microT 2023: including predicted targets of virally encoded miRNAs. *Nucleic Acids Res.* **51**, W148–W153 (2023).
95. Gaidatzis, D., van Nimwegen, E., Hausser, J. & Zavolan, M. Inference of miRNA targets using evolutionary conservation and pathway analysis. *BMC Bioinform.* **8**, 69 (2007).
96. Mu, W. & Zhang, W. Bioinformatic resources of microRNA sequences, gene targets, and genetic variation. *Front. Genet.* **3**, 31 (2012).
97. Betel, D., Wilson, M., Gabow, A., Marks, D. S. & Sander, C. The microRNA.org resource: targets and expression. *Nucleic Acids Res.* **36**, D149–D153 (2008).
98. Chen, Y. & Wang, X. miRDB: an online database for prediction of functional microRNA targets. *Nucleic Acids Res.* **48**, D127–D131 (2019).
99. Anders, G. et al. doRiNA: a database of RNA interactions in post-transcriptional regulation. *Nucleic Acids Res.* **40**, D180–D186 (2012).
100. Kertesz, M., Iovino, N., Unnerstall, U., Gaul, U. & Segal, E. The role of site accessibility in microRNA target recognition. *Nat. Genet.* **39**, 1278–1284 (2007).
101. Grimson, A. et al. MicroRNA targeting specificity in mammals: determinants beyond seed pairing. *Mol. Cell* **27**, 91–105 (2007).
102. Xu, T. et al. miRBaseConverter: an R/Bioconductor package for converting and retrieving miRNA name, accession, sequence and family information in different versions of miRBase. *BMC Bioinform.* **19**, 514 (2018).
103. Langfelder, P. & Horvath, S. WGCNA: an R package for weighted correlation network analysis. *BMC Bioinform.* **9**, 559 (2008).
104. Yao, Z. et al. A taxonomy of transcriptomic cell types across the isocortex and hippocampal formation. *Cell* **184**, 3222–3241.e3226 (2021).
105. Shannon, P. et al. Cytoscape: a software environment for integrated models of biomolecular interaction networks. *Genome Res.* **13**, 2498–2504 (2003).
106. R: A language and environment for statistical computing v. 4.4.0 (2024).

Acknowledgments

This work was supported by the Natural Sciences and Engineering Research Council of Canada (Discovery Grant; #RGPIN-05604), Canadian Institutes for Health Research (Project Grant; #PJT-190170) and the Brain Canada Foundation (2020 Future Leaders in Canadian Brain Research) to N.G., and the Ontario Graduate Scholarship to A.M.Z. Computations were performed on resources and with support provided by the Center for Advanced Computing (CAC) at Queen’s University in Kingston, Ontario. The CAC is supported in part by funding from Queen’s University, the Digital Research Alliance of Canada and the Government of Ontario. The funders had no role in study design, data collection and analysis, decision to publish, or preparation of the manuscript.

Author contributions

A.M.Z., C.D.O., D.G.T., H.C., H.G., Q.L.D., and N.G. conceived and planned analyses. Computational analyses were performed by A.M.Z., with support from Z.Y.F. Experiments were performed and analyzed by C.D.O. Interpretation of findings was conducted by A.M.Z., C.D.O., Q.L.D., and N.G. Paper preparation was largely performed by A.M.Z., C.D.O., and N.G. The figures were prepared by A.M.Z. and C.D.O. All authors reviewed the results and contributed to the final paper.

Competing interests

D.G.T. is currently an employee of Olink Proteomics AB, however, the published work was done prior to this employment and does not involve/promote any of Olink’s materials or point of view. H.C. is currently an employee of Geneseeq Technology Inc., however, the published work was done prior to this employment and does not involve/promote any of Geneseeq’s materials or points of view. H.G. is currently an employee at Caruta Therapeutics, however, the published work was done prior to this employment and does not involve/promote any of Caruta’s materials or points of view. All other authors declare no competing interests.

Additional information

Supplementary information The online version contains supplementary material available at <https://doi.org/10.1038/s42003-025-08371-7>.

Correspondence and requests for materials should be addressed to Qingling Duan or Nader Ghasemlou.

Peer review information *Communications Biology* thanks Nicolas Cermakian for their contribution to the peer review of this work. Primary Handling Editor: Benjamin Bessieres. A peer review file is available.

Reprints and permissions information is available at <http://www.nature.com/reprints>

Publisher's note Springer Nature remains neutral with regard to jurisdictional claims in published maps and institutional affiliations.

Open Access This article is licensed under a Creative Commons Attribution-NonCommercial-NoDerivatives 4.0 International License, which permits any non-commercial use, sharing, distribution and reproduction in any medium or format, as long as you give appropriate credit to the original author(s) and the source, provide a link to the Creative Commons licence, and indicate if you modified the licensed material. You do not have permission under this licence to share adapted material derived from this article or parts of it. The images or other third party material in this article are included in the article's Creative Commons licence, unless indicated otherwise in a credit line to the material. If material is not included in the article's Creative Commons licence and your intended use is not permitted by statutory regulation or exceeds the permitted use, you will need to obtain permission directly from the copyright holder. To view a copy of this licence, visit <http://creativecommons.org/licenses/by-nc-nd/4.0/>.

© The Author(s) 2025